# Fabrication of 3D Oriented MOF Micropatterns with Anisotropic Fluorescent Properties

*Miriam de J. Velásquez-Hernández, Mercedes Linares-Moreau, Lea A. Brandner, Benedetta Marmiroli, Mariano Barella, Guillermo P. Acuna, Simone Dal Zilio, Margot F. K. Verstreken, Dmitry E. Kravchenko, Oliver M. Linder-Patton, Jack D. Evans, Helmar Wiltsche, Francesco Carraro, Heimo Wolinski, Rob Ameloot, Christian Doonan,\* and Paolo Falcaro\**

Micropatterning crystalline materials with oriented pores is necessary for the fabrication of devices with anisotropic properties. Crystalline and porous metal–organic frameworks (MOFs) are ideal materials as their chemical and structural mutability enables precise tuning of functional properties for applications ranging from microelectronics to photonics. Herein, a patternable oriented MOF film is designed: by using a photomask under X-ray exposure, the MOF film decomposes in the irradiated areas, remaining intact in the unexposed regions. The MOF film acts simultaneously as a resist and as functional porous material. While the heteroepitaxial growth from aligned $Cu(OH)_2$ nanobelts is used to deposit oriented MOF films, the sensitivity to radiation is achieved by integrating a brominated dicarboxylate ligand ($Br_2BDC$) into a copper-based MOF $Cu_2L_2DABCO$ (DABCO = 1,4-diazabicyclo[2.2.2]octane; L = $BDC/Br_2BDC$). The lithographed samples act as diffraction gratings upon irradiation with a laser, thus confirming the quality of the extended MOF micropattern. Furthermore, the oriented MOF patterns are functionalized with fluorescent dyes. As a result, by rotating the polarization angle of the laser excitation, the alignment of the dye in the MOF is demonstrated. By controlling the functional response to light, this MOF patterning protocol can be used for the microfabrication of optical components for photonic devices.

## 1. Introduction

Metal–organic frameworks (MOFs) are a class of extended materials formed via the self-assembly of metal ions and multitopic organic linkers.[1,2] These building blocks can be carefully selected to tailor the MOFs' physical properties, including pore volume, accessible surface area, chemical stability, conductivity, refractive index, and fluorescence.[1,2] This precise synthetic control of their structure and functionality renders MOFs an attractive platform material for miniaturized devices such as chemical sensors,[3,4] microelectronic components, and photonic devices.[5–9] The fabrication of devices at these scales typically requires the MOF component to be processed as supported thin films[10–14] so that its single crystal properties can be translated over a specified area. To this end, a recent and significant advance in MOF film research[15] showed that oriented polycrystalline MOF films can be prepared at commercially relevant scales[16]

These films were synthesized from prealigned metal hydroxide nanostructures ($Cu(OH)_2$ nanobelts, NBs) where the ceramic

M. de J. Velásquez-Hernández, M. Linares-Moreau, L. A. Brandner, F. Carraro, P. Falcaro
Institute of Physical and Theoretical Chemistry
Graz University of Technology
Graz 8010, Austria
E-mail: paolo.falcaro@tugraz.at

B. Marmiroli
Institute of Inorganic Chemistry
Graz University of Technology
Graz 8010, Austria

M. Barella, G. P. Acuna
Department of Physics
University of Fribourg
Fribourg CH-1700, Switzerland

S. D. Zilio
Istituto Officina dei Materiali CNR
Edificio MM-SS
Basovizza, Trieste 34149, Italy

M. F. K. Verstreken, D. E. Kravchenko, R. Ameloot
Centre for Membrane Separations, Adsorption, Catalysis and Spectroscopy for Sustainable Solutions (cMACS)
KU Leuven, Leuven 3001, Belgium

material simultaneously acts as a metal source and directs epitaxial growth of the aligned MOF crystals.

While the growth of oriented MOF films represented a milestone toward the integration of MOFs into microdevices, further progress requires positioning protocols that confine portions of the MOF films into predefined micrometer-sized areas (micropatterning) on substrates.[7] However, a limited number of studies describing patterning protocols for MOF films have been reported, and importantly, the fabrication of micropatterns composed of 3D-oriented crystals has not been shown.[12,17–19] Nevertheless, this combination of properties is highly desirable in porous-material-based technologies.[5,20] The majority of MOF micropatterning protocols use photolithography,[12,21] which can be summarized by the following steps: 1) deposition of a photoresist, 2) exposure of the resist to UV radiation followed by developing, 3) growth of a MOF film, 4) etching of the residual resist, and thus the MOF crystals, from selected regions (liftoff).[22] The main advantage of photolithography is its compatibility with the majority of the current industrial microfabrication techniques.[5,10] However, a drawback of this approach is that the etching step could lead to blockage or decomposition of the MOF pore structure.[23–26] To avoid these issues, Ameloot and co-workers[27] synthesized randomly oriented zeolitic imidazolate framework (ZIF) films comprised of halogenated organic linkers. Exposing these ZIF films to hard X-rays results in homolytic cleavage of the C–Cl bond: this effect was studied in chlorinated ZIF-71 through X-ray photoelectron spectroscopy measurements at different irradiation doses.[27] The resulting reactive halogenated species would lead to selective decomposition of the irradiated areas of the MOF film, which could be easily removed via dissolution. Inspired by this concept, we hypothesized that a resist-free strategy for micropatterning could be applied to halogen-functionalized carboxylate-based MOF films with oriented pore channels. This strategy would combine bottom-up self-assembly of an oriented MOF film and top-down lithography to enable the fabrication of microdevices with anisotropic properties.

Herein, we report the microfabrication of oriented MOF patterns from aligned MOF films by using a resist-free protocol. Highly aligned $Cu(OH)_2$ nanobelt films were used as a sacrificial template to induce the heteroepitaxial growth of $Cu_2L_2DABCO$, where DABCO = 1,4-diazabicyclo[2.2.2]octane and L = brominated dicarboxylate ligand ($Br_2BDC$) and/or 1,4-benzenedicarboxylate ligand (BDC), with in-plane orientation

(**Scheme 1**a). $Br_2BDC$ was selected because bromine will result in a larger number of X-ray photons absorbed compared to chlorine, and on average the dissociation energy of C–Br bonds is about 20% lower than for C–Cl bonds.[28] Thus, we theorized that the hard-X-ray-induced cleavage would efficiently occur in the case of the $Br_2BDC$ linker. Additionally, the choice of $Cu_2L_2DABCO$ (L = $Br_2BDC$ and/or BDC) was inspired by previous reports on isostructural Cu-paddlewheel surface-mounted MOFs (SURMOFs) composed of a brominated dicarboxylic acid and DABCO.[29]

In this work, a mixed-linker ($Br_2BDC$ and/or BDC) strategy was required to ensure in-plane orientation and homogeneity of the MOF films (Scheme 1b). The resultant MOF films were exposed to hard X-rays through a lithography mask (deep X-ray lithography, DXRL) (Scheme 1c). Subsequently, the MOF patterns were developed by selective dissolution of the irradiated area in a mixture of $MeOH/H_2O/AcOH$ (Scheme 1d). The obtained patterns were characterized by X-ray diffraction (XRD), Fourier transform infrared (FT-IR), Raman spectroscopy, and scanning electron microscopy (SEM). Finally, we incorporated a fluorescent dye within the aligned pore channels of the MOF patterns and measured the resulting anisotropic photoluminescent response.

## 2. Results and Discussion

### 2.1. Synthesis of $Cu_2L_2DABCO$ Films (L = BDC/$Br_2BDC$)

Mixed-linker MOF films were prepared by depositing aligned $Cu(OH)_2$ NBs on a silicon substrate according to our previously reported protocol (see the Supporting Information for details).[16] The $Cu(OH)_2$ NB films were then immersed in 10 mL of a methanolic solution containing DABCO and the dicarboxylate linkers $Br_2BDC$ and BDC in different molar ratios to yield a set of films composed of $Cu_2[(Br_2BDC)_x(BDC)_{1-x}]_2DABCO$ ($x = Br_2BDC/(BDC + Br_2BDC)$). We will refer to these samples according to the nominal mole ratio of the dicarboxylate ligands, e.g., **B0** for $x = 0$, **B94** for $x = 0.94$, and **B100** for $x = 1$. Finally, the converted film was removed from the reaction medium, washed with ethanol, and dried under $N_2$ flow. It is important to note that the use of other reported Cu-based insoluble precursors (i.e., $Cu_2(OH)_3NO_3$) employed for patterns of Cu-based MOFs,[30] on our hands, does not afford 3D oriented MOF films (data not shown).

The morphology and homogeneity of the $Cu_2[(Br_2BDC)_x(BDC)_{1-x}]_2DABCO$ films were examined by SEM. Microscopy images of sample **B0** indicate the formation of a homogeneous MOF coating consisting of aligned intergrown microcrystals with prism-like morphology and an average crystal size of ≈250 nm (**Figure 1**a). By contrast, sample **B100** showed isolated cubic microcrystals with an average size of ≈1.7 μm. Additionally, **B100** was found to be a nonhomogeneous film comprised of twinned crystals (Figure 1a and Figure S1 (Supporting Information)). The loss of homogeneity when switching from 100% BDC to 100% $Br_2BDC$ underscores the influence of the linker functionalization on the crystal growth process. We note that Zhuang and co-workers[29] have previously reported the effect that substituents on BDC linkers have on the fabrication of MOF films (SURMOFs). Based on the lack of film homogeneity

O. M. Linder-Patton, J. D. Evans, C. Doonan
Department of Chemistry
The University of Adelaide
Adelaide, South Australia 5005, Australia
E-mail: christian.doonan@adelaide.edu.au

H. Wiltsche
Institute of Analytical Chemistry and Food Chemistry
Graz University of Technology
Graz 8010, Austria

H. Wolinski
Institute of Molecular Biosciences
Field of Excellence BioHealth
University of Graz
Graz 8010, Austria

**ADVANCED
SCIENCE NEWS**

www.advancedsciencenews.com

**ADVANCED
MATERIALS**

www.advmat.de

and the presence of twin crystals, **B100** (100% $Br_2BDC$) was rated as a MOF film unsuitable for the fabrication of high-quality micropatterns (see **Table 1**).

To achieve a homogeneous MOF coating (such as **B0**, vide supra) while containing the photoactive $Br_2BDC$ linker, we explored the preparation of mixed-linker MOF films synthesized from both BDC and $Br_2BDC$ linkers. We found that a molar ratio of 6% of BDC and 94% of $Br_2BDC$ (**B94**), in the converting solution, was the highest $Br_2BDC$ content that yielded a continuous and homogeneous film. SEM images of **B94** are presented in Figure 1a and show close-packed intergrown MOF crystals with prism-shape morphology and an average size of ≈400 nm.

The elemental composition of **B0**, **B94**, and **B100** was determined by energy-dispersive X-ray spectroscopy. The average weight percentage of Br was calculated for the different samples and compared by using a sputtered Au coating as an internal reference (see Figure S2a in the Supporting Information). The Br/Au weight ratios obtained for **B0**, **B94**, and **B100** are $(0.01 \pm 0.01)$, $(0.11 \pm 0.01)$, and $(0.24 \pm 0.02)$, respectively. These data indicate the presence of Br in samples **B94** and **B100**, with a relative Br content of ≈46% for **B94** with respect to **B100**. Thus, sample **B94** is approximately a 50/50 mixture of brominated and nonbrominated BDC linkers. Raman spectroscopy analysis provides further evidence that **B94** contains both BDC and $Br_2BDC$. Figure 1b shows that the Raman spectra obtained from **B0** and **B100** possess marked differences in the vibrational modes of the respective carboxylate linkers. For instance, the band associated with the ring stretching mode (C=C) is centered at 1611 $cm^{-1}$ in sample **B0**, whereas for **B100**, this band is shifted to 1592 $cm^{-1}$.[31–33] Additionally, the mode assigned to $\nu(C–CH_3)$ is centered at 1137 $cm^{-1}$ in **B0**, while in **B100** this band is located at 1168 $cm^{-1}$. As expected, the spectrum obtained from the mixed-linker MOF film **B94** displays a superposition of the bands observed in both single-linker counterparts (**B0** and **B100**) (Figure 1b). FT-IR spectroscopy analysis of sample **B0** showed bands assigned to the symmetric and asymmetric stretching vibration of the $-COO^-$ group centered at 1392 and 1625 $cm^{-1}$, respectively (Figure 1c and Figure S2b (Supporting Information)).[31] However, for samples **B94** ($\nu_s$ 1398 $cm^{-1}$, $\nu_{as}$ 1635 $cm^{-1}$) and **B100** ($\nu_s$ 1404 $cm^{-1}$, $\nu_{as}$ 1639 $cm^{-1}$), those vibration bands are blueshifted.

**Table 1.** Summary of the properties of the different MOF films. From these, **B94** is the only suitable film for X-ray lithography.

| Sample | Homogeneity of the MOF film | 3D crystalline alignment | Sensitivity to X-rays (crystalline structure) |
|---|---|---|---|
| **B0** | Yes | Yes | Low |
| **B94** | Yes | Yes | High |
| **B100** | No (isolated crystals) | No (twin crystals) | High |

The shift in the $-COO^-$ vibrational bands observed for **B94** can be attributed to the presence of $Br_2BDC$ within the crystalline film (Figure 1c). This blueshift is due to the electron-withdrawing effect of the $-Br$ substituents of the BDC linker.[29]

The orientation and alignment of **B0**, **B94**, and **B100** were assessed by X-ray diffraction (Figure 1d). The out-of-plane XRD pattern (OP-XRD) of sample **B0** exhibits an intense diffraction peak at $2\theta = 8.2°$ ascribed to the (010) planes. This result agrees with previous reports for the in-plane orientation of heteroepitaxially grown $Cu_2(BDC)_2DABCO$ on oriented $Cu(OH)_2$ NBs.[15,34] By contrast, the OP-XRD pattern of sample **B100** displays two diffraction peaks at $2\theta \approx 8.2°$ and $2\theta \approx 9.2°$, these reflections are associated with the (010) and (001) planes, respectively. The presence of the additional peak at $2\theta \approx 9.2°$ indicates that replacing BDC with $Br_2BDC$ alters the orientation-controlled growth of the MOF crystals. This change leads to the loss of the in-plane orientation typically found for $Cu_2(BDC)_2DABCO$ (see **B0**). Again, **B100** showed properties that make the 100% $Br_2BDC$ unsuitable for the fabrication of 3D-oriented micropatterns (see Table 1). However, the mixed-linker strategy employed to synthesize sample **B94** affords a diffraction pattern analogous to the one observed for sample **B0** with a dominant reflection at 8.2° ascribed to the (010) plane. This result indicates that in-plane orientation can be achieved by adding only 6% mol of BDC to the reaction media.

To demonstrate the epitaxial relationship between the $Cu(OH)_2$ NBs and the MOF in sample **B94**, we investigated the azimuthal angle ($\varphi$) dependence in the intensity profiles of the (002) reflection from $Cu(OH)_2$ ($2\theta = 34.03°$), and the
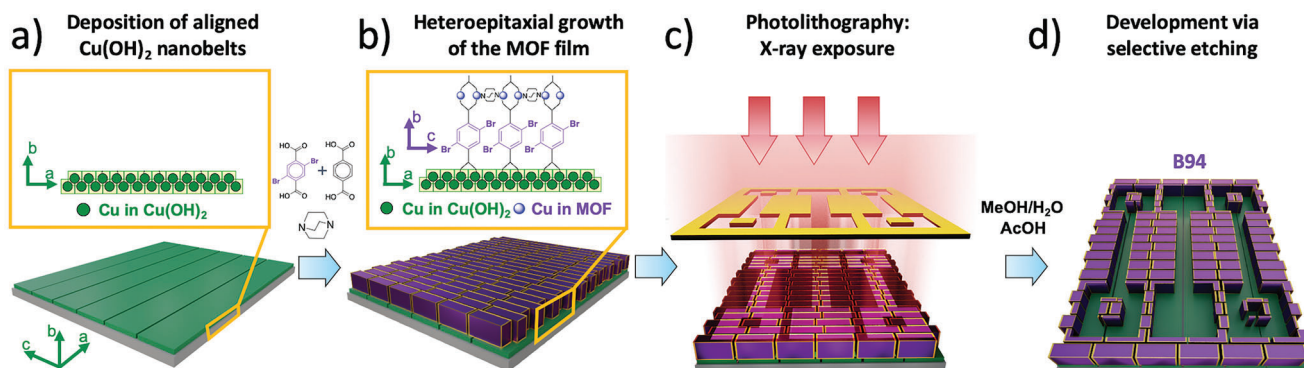


**Scheme 1.** Scheme illustrating the resist-free patterning of oriented MOF films and the different fabrication steps. a) A film of aligned $Cu(OH)_2$ nanobelts is deposited on a silicon (Si) wafer. b) The $Cu(OH)_2$ nanobelts are used as a sacrificial template for the heteroepitaxial growth of an oriented Cu-based MOF film with nominal formula $Cu_2[(Br_2BDC)_{0.94}(BDC)_{0.06}]_2DABCO$. c) The MOF film is exposed to deep X-rays through a lithography mask. d) The exposed MOF film is soaked in a mixture of $MeOH/H_2O/AcOH$: the selective dissolution of MOF in the exposed areas affords the development of high-quality patterns with oriented pores.
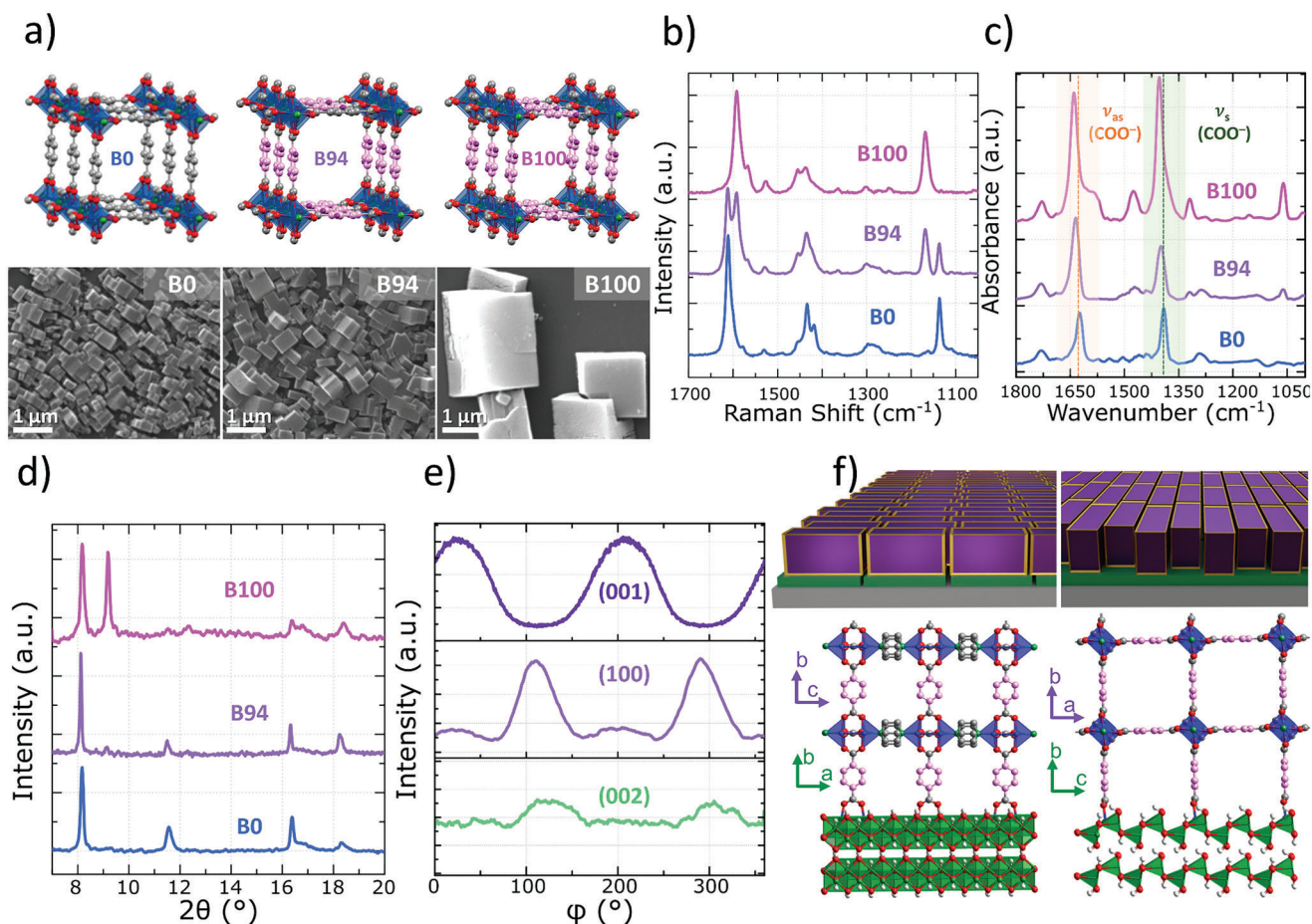
**2211478 (3 of 10)**

**Figure 1.** a) SEM images of the $Cu_2[(Br_2BDC)_x(BDC)_{1-x}]_2DABCO$ films **B0** ($x = 0$), **B94** ($x = 94$), and **B100** ($x = 100$) grown on $Cu(OH)_2$ NB films. b) Characterization of **B0**, **B94**, and **B100** by Raman spectroscopy. c) FT-IR spectra in the region of the $-COO^-$ stretching modes. d) Out-of-plane XRD patterns collected for the **B0**, **B94**, and **B100** films. e) Azimuthal angle dependence of intensity profiles of the (002) reflection of $Cu(OH)_2$ NBs at a diffraction angle of 34.03°, and the reflections (100) and (001) of the mixed-linker MOF film **B94** taken at diffraction angles of 8.2° and 9.2°, respectively. f) Schematics of the heteroepitaxial growth of $Cu_2[(Br_2BDC)_x(BDC)_{1-x}]_2DABCO$ films; showing two different views of the interface between the Cu–MOF and the $Cu(OH)_2$ substrate, one parallel and one perpendicular to the longitudinal axis of the $Cu(OH)_2$ NBs.

(100) and (001) reflections of $Cu_2[(Br_2BDC)_x(BDC)_{1-x}]_2DABCO$ centered at $2\theta \approx 8.2°$ and $2\theta \approx 9.2°$ (see Figure 1e). The $\varphi$ scan profile shows that the two maxima of the (100) MOF reflection ($\varphi = 110°$ and $290°$) are coincident with the maxima of the reflection (002) of the $Cu(OH)_2$ NBs (Figure 1e lower panel). This observation confirms the heteroepitaxial growth of the mixed-linker MOF crystals, where the 1D pore channels (along the $c$-axis) align parallel to the $a$-axis of the $Cu(OH)_2$ NBs (Figure 1f).[15] The thickness and roughness of the films were studied by atomic force microscopy (AFM), showing that **B0** and **B94** exhibit a comparable thickness of $\approx 400$ nm (Figure S14 and Table S2, Supporting Information).

## 2.2. X-ray Sensitivity and Optimization of Patterning Conditions

The photosensitivity of the oriented MOF films **B0**, **B100**, and **B94** was examined using hard X-rays from a synchrotron source. We performed a dose matrix and exposed MOF films to doses in the 0–6995 J cm$^{-2}$ range (see Figures S3 and S7 in the Supporting

Information). For each sample, we characterized the chemical and structural changes of the MOF films by FT-IR spectroscopy and XRD (**Figure 2**a–e). FT-IR spectra were collected before and after each exposure (7 doses), and the relative change of the symmetric $-COO^-$ stretching mode (at 1392 cm$^{-1}$ for **B0**, 1398 cm$^{-1}$ for **B94**, and 1404 cm$^{-1}$ for **B100**, details in the Supporting Information) was calculated. Each of the MOF films showed a decrease in the symmetric $-COO^-$ stretch band with incremental X-ray doses (Figure 2d). **B100** exhibits the highest sensitivity, with a 70% loss in intensity after a total dose of 1748 J cm$^{-2}$. The decrease in intensity observed for **B0** is less significant (15%), while **B94** shows an intermediate value of $\approx 50\%$. As expected, the mixed-linker MOF **B94** shows enhanced sensitivity to X-rays compared to its nonbrominated counterpart **B0**. XRD was collected before and after X-ray exposure, and the change in the integrated area of the diffraction peak corresponding to the (010) reflection of the MOF ($2\theta \approx 8.2°$) was calculated, see Figure 2e. Analogous to the FT-IR data, the loss in crystallinity was correlated to the $Br_2BDC$ linker content. The nonbrominated film **B0** shows, especially at low doses, a limited loss in diffraction
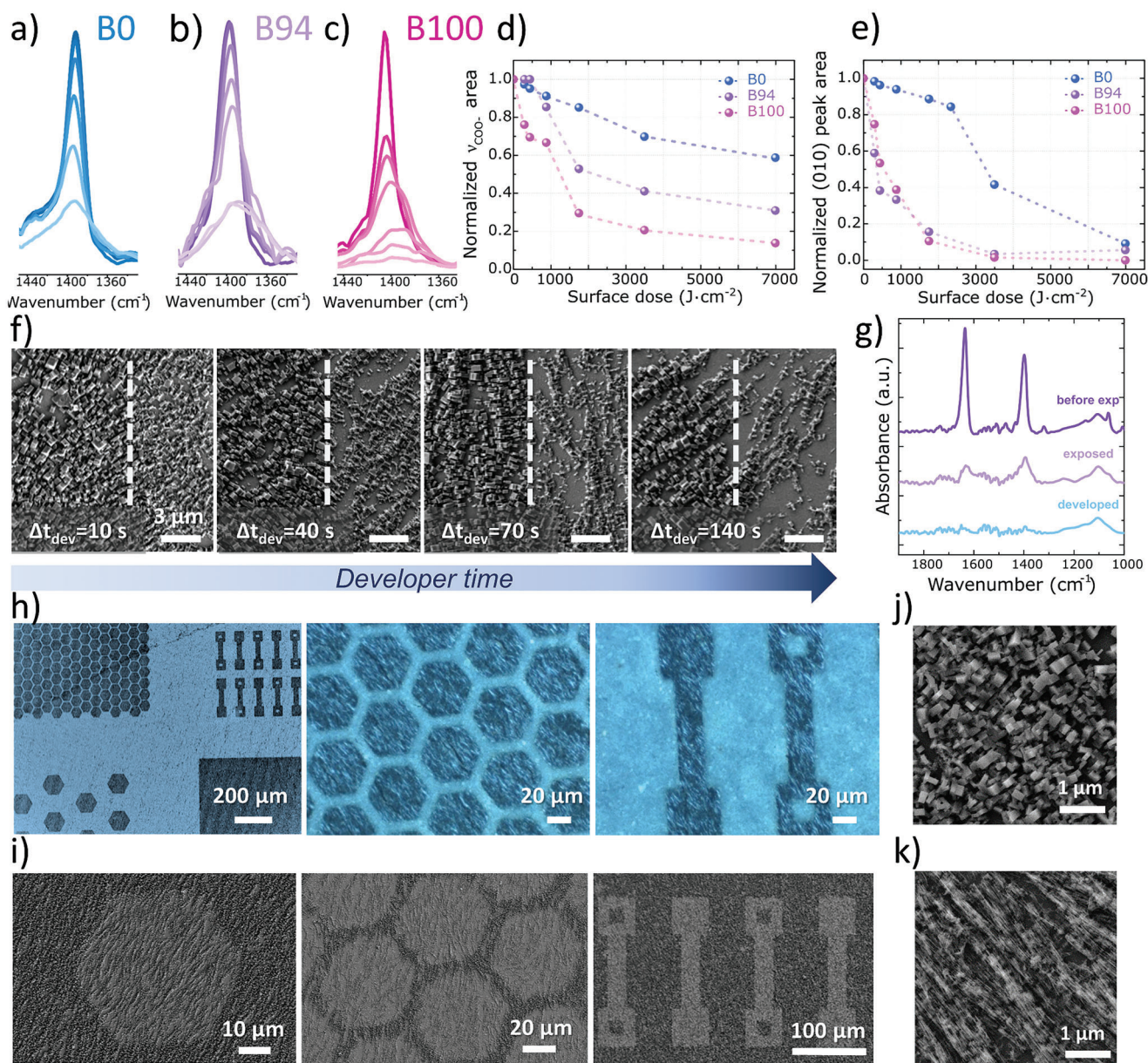
**Figure 2.** a–c) FT-IR spectra of **B0** (a), **B94** (b), and **B100** (c) after increasing X-ray doses. d) Dose matrix following the normalized intensity change of the symmetric −COO⁻ stretch for increasing X-ray doses. e) Dose matrix following the normalized integrated intensity of the MOF's (010) reflection measured at a diffraction angle of $2\theta = 8.2°$, for each X-ray surface dose. f) SEM images of the edge of a patterned **B94** sample with different times of exposure to the developer solution. g) FT-IR spectra of a sample before and after exposure to the selected 1748 J cm⁻² dose, and after developing. h) Optical microscopy and i) SEM images of different patterns. j,k) High-magnification images of the nonexposed (j) and exposed (k) regions of **B94** after etching. The images in (h–k) correspond to samples deposited on double-layered $Cu(OH)_2$ films.

intensity, while the **B94** and **B100** systems show a pronounced and similar trend in the loss of the diffraction intensity. For example, both **B94** and **B100** show an approximate intensity loss of 70% after an X-ray dose of 874 J cm⁻² indicating the partial decomposition of the MOF crystalline structure. Based on the FT-IR and XRD data, the use of $Br_2BDC$ as a MOF building block clearly provides increased X-ray sensitivity. Although the fully brominated system **B100** shows the highest sensitivity, the lack of film homogeneity (see Figure 1a and Figure S1 in the Supporting Information) makes this MOF system unsuitable for the

fabrication of high-quality patterns. By contrast, the **B94** mixed-linker system affords high in-plane crystalline orientation, film homogeneity, and high chemical and structural sensitivity to X-rays (see Table 1).

As a result of the **B94** film properties, we focused our effort on these films and we investigated suitable etching conditions for the fabrication of oriented patterns at the micrometric scale. Based on the FT-IR analysis of the dose matrix, we found that a dose of 1748 J cm⁻² was suitable to maximize the chemical changes between the irradiated and nonirradiated areas (see

**ADVANCED
SCIENCE NEWS**

www.advancedsciencenews.com

**ADVANCED
MATERIALS**

www.advmat.de

Figures S3 and S7 in the Supporting Information). Thus, at this dose, we tested a variety of etching solutions giving priority to green solvents (e.g., water, ethanol, methanol, and their mixtures). To this end, we found that a mixture of acetic acid (0.02 mL), methanol (9 mL), and water (1 mL) dissolved the irradiated areas within tens of seconds (see the Experimental Section). Then, we studied the influence of the etching time using this developer solution (Figure 2f). We found that immersion times exceeding 1 min etched the MOF crystals in both the exposed and nonexposed regions of the film, leading to an overdeveloped pattern and the removal of the residual $Cu(OH)_2$ NBs (see Figure 2f). However, a 40 s immersion provides optimal contrast between exposed and masked regions for the 1748 J cm$^{-2}$ X-ray dose. For this immersion time, the unexposed regions do not show evident changes in morphology, structure, or chemical composition, but the MOFs in the exposed areas are selectively removed (Figure 2g,j, Figure S4 and Figure S14, Supporting Information). To improve the long-range homogeneity of the **B94** MOF film, MOF samples were grown on double layers of $Cu(OH)_2$ NB films on either Si or quartz substrates (see Figures S5 and S15 in the Supporting Information for details). We then employed the optimized exposure dose and etching conditions to fabricate oriented MOF patterns using a suitable photomask (Figure S6, Supporting Information). The resulting **B94** patterns were analyzed with polarized optical microscopy and SEM. Close analysis of these data presented in Figure 2h,i confirms the successful fabrication of homogeneous and well-defined micropatterns with diverse shapes and sizes (see Figure 2h,i and Figures S8 and S9 in the Supporting Information). Furthermore, the SEM images in Figure 2j reveal the presence of oriented MOF crystals. In the etched regions (Figure 2k), it is possible to observe elongated nanostructures that are engendered by residual $Cu(OH)_2$ nanobelts. The alignment of the MOF crystals in the patterns was confirmed by using XRD to measure the dependence of the intensity profiles on the azimuthal angle ($\varphi$) (see Figure S10b in the Supporting Information). Chemical maps collected with a Raman microscope further show the localization of the MOF vibrational modes following the pattern features (Figure S11, Supporting Information). The quality of the fabricated MOF micropatterns, over millimeter scales, was ascertained by the appearance of constructive and destructive interference spots upon illumination with a 650 nm red laser source (see diffraction patterns obtained with a simple laser pointer in **Figure 3**a and Figure S12 and Video S1 in the Supporting Information). We note that optical diffraction gratings are suitable components for sensing and photonic applications.[27,35]

Finally, we examined the MOF film porosity before and after patterning by measuring methanol isotherms for samples deposited on quartz crystal microbalance substrates. The unexposed and patterned **B94** films both show an approximate uptake of 33 mg g$^{-1}$ of methanol (see details in Figure S13 in the Supporting Information); this value is consistent with the reported values on similar microporous systems.[29,36]

Collectively, our data demonstrate that: 1) oriented $Br_2BDC/BDC$ Cu–MOF can be used as a photosensitive film for photolithographic processes; 2) after the entire patterning protocol, the MOF film properties (chemical and structural integrity, porosity, and crystalline orientation) are preserved in the MOF micropatterns.

## 2.3. Anisotropic Fluorescence Response of Micropatterned Regions by Guest Incorporation

To further explore the potential of oriented MOF patterns for photonics, we immobilized a fluorescent guest molecule, difluoro{2-[(3,5-dimethyl-2*H*-pyrrol-2-ylidene-*N*)methyl]-3,5-dimethyl-1*H*-pyrrolato-*N*}boron (BODIPY, BPY), within the oriented pore channels. Preferential alignment of BPY within the MOF micropatterns (**BPY@B94**) was attempted via two different procedures: in situ encapsulation (one-pot synthesis, named **encBPY@B94**) and post-infiltration (two steps synthesis, named **postBPY@B94**). The one-pot encapsulation of the dye during the MOF growth was performed by immersing the $Cu(OH)_2$ film in a methanolic solution containing BPY, $Br_2BDC$, BDC, and DABCO (see the Experimental Section). Then, the aforementioned photolithographic process, vide supra, was followed to yield a fluorescent MOF pattern, **encBPY@B94**, with anisotropic photoresponse properties. On the other hand, the post-infiltration strategy was as follows: 1) we selected a DXRL micropatterned **B94** sample on silicon, 2) a MOF activation procedure was carried out, and 3) the activated MOF pattern was immersed in a solution of BPY in dried chloroform (CHCl$_3$) (see the Experimental Section for details) to afford **postBPY@B94**. To compare BPY immobilized in the MOF samples via i) the coencapsulation and ii) the post-infiltration, we quantified the boron content (i.e., boron is a constituent element of BPY) in **encBPY@B94** and **postBPY@B94** samples by inductively coupled plasma-optical emission spectrometry (ICP-OES). This analysis indicates the presence of boron in **encBPY@B94** (200 ± 10 ppm) and **postBPY@B94** (190 ± 10 ppm) suggesting that both methods can be used for the successful immobilization of a guest dye in the porous crystals (see Table S1 in the Supporting Information). We performed molecular simulations and measured the pore size distribution (see the Supporting Information) that further prove that BPY can fit and orient inside the brominated MOF's pores (Figures S20–S24 and Tables S3 and S4, Supporting Information). AFM measurements show that the morphology of **encBPY@B94** and **postBPY@B94** is comparable to **B94** (Figure S19, Supporting Information).

Confocal laser scanning microscopy (CLSM) and widefield fluorescence microscopy revealed that the fluorophore was homogeneously incorporated into the MOF patterns prepared with both protocols (Figure 3b–d and Figures S16–S18 and Videos S2 and S3 (Supporting Information)). The anisotropic optical response of **encBPY@B94** and **postBPY@B94** patterned samples was then assessed via widefield fluorescence microscopy.[37] Both **encBPY@B94** and **postBPY@B94** were excited with a 488 nm laser, while the detection range was $\lambda > 500$ nm (see the Experimental Section for further details). Polarization-resolved measurements were carried out by rotating the linear polarization of the laser excitation to cover a range of 180°. The fluorescence intensity was averaged over an area of $60 \times 60$ μm$^2$ for different polarization angles (Figure 3e–h). Figure 3f shows fluorescent intensity plots as a function of the polarization angle for **encBPY@B94** and for the control samples, **B94** and $Cu(OH)_2$ films. The results show that the mean value of the fluorescence signal from the **encBPY@B94** samples is more intense than the control samples without BPY ($\approx$400 times higher for both the unexposed MOF and $Cu(OH)_2$ films), indicating the success of the

**ADVANCED
SCIENCE NEWS**

www.advancedsciencenews.com
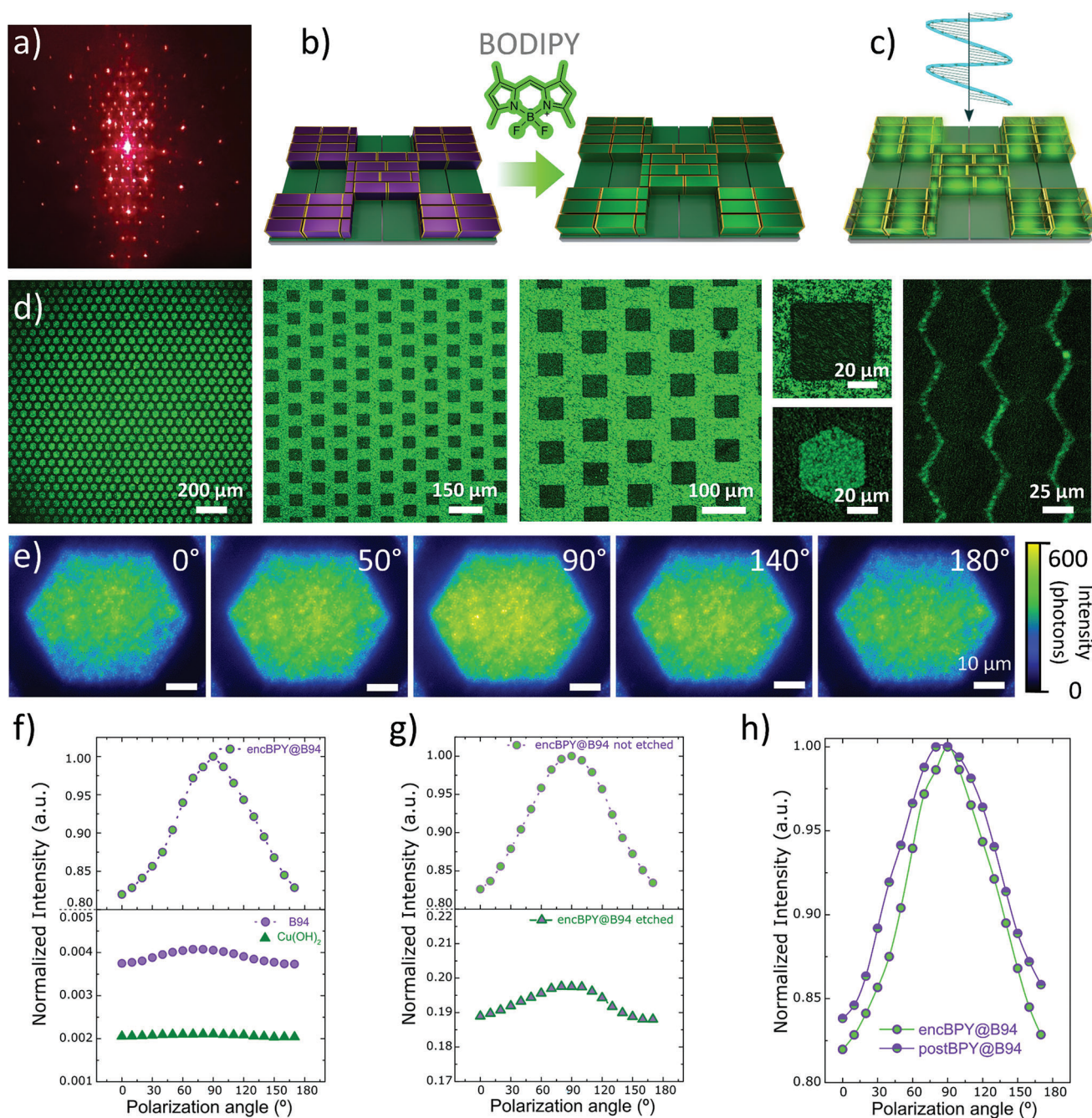
**ADVANCED
MATERIALS**

www.advmat.de

**Figure 3.** a) Diffraction pattern obtained by exposing the lithographed **B94** samples to a red laser ($\lambda = 650$ nm). b,c) Schematic representation of the BPY infiltration process and polarized photoresponse measurement. d) Confocal laser scanning microscopy (CLSM) images of the fluorescent patterns from the **encBPY@B94** sample acquired using different zoom factors. e) Fluorescence microscopy images obtained by rotating the polarization of the excitation laser at different angles. f–h) Plots of integrated fluorescence intensity as a function of the polarization angle of the source, comparing **encBPY@B94** films, **B94** film, and $Cu(OH)_2$ substrate (f), etched and nonetched regions of a patterned **encBPY@B94** film (g), and **encBPY@B94** and **postBPY@B94** samples (h).

encapsulation protocol. The polarization-resolved measurement shows that the fluorescence signal from **encBPY@B94** has a minimum at 0° polarization, a maximum at 90°, and a minimum at 180°. This trend can be justified by the preferential alignment of the dye's dipole moment with the aligned MOF pores and significantly exceeds the fluorescent background resulting from

spatially disordered dye molecules. The fluorescent emission of patterned **encBPY@B94** and parental **encBPY@B94** films used for the photolithography process showed similar anisotropic photoresponses (Figure 3e). A large difference in the emission intensity was also observed for the etched regions of the lithographed **encBPY@B94**. The exposed residual $Cu(OH)_2$ NBs showed a

reduced mean fluorescence signal that is ≈20% of the intensity measured in the masked area of the **encBPY@B94** patterns (Figure 3g). Importantly, in the case of the **encBPY@B94** samples, the fluorescence microscopy results highlight that the fluorescent properties of the dye were preserved after the entire microfabrication process. The fluorescence emission versus the polarization angle for **postBPY@B94** and **encBPY@B94** engenders a similar anisotropic fluorescence response, which underscores the versatility of the fabrication procedure (Figure 3h) for the immobilization of a model–fluorescent guest. We note that the successful incorporation of BPY inside the pores of the patterned films for the **postBPY@B94** is further proof of the integrity of the porous framework after the patterning protocol (see Figure 3h and Figure S17 in the Supporting Information). Additionally, we observed that the infiltration with BPY is only possible after performing an activation procedure to remove the solvent molecules occluding the MOF's pores (Figure S18, Supporting Information).

As **B94** can be used as a matrix for the orientation of BPY, and potentially other guests for applications where localized anisotropic properties are desirable, we tested the stability of the **B94** films to temperature and humidity. We exposed **B94** films to various temperatures (from 25 to 300 °C, 1 h) and different relative humidity (RH = 0%, 50%, and 80%, from 1 to 7 days). The chemical and structural stability was monitored by FT-IR and XRD. The thermal treatment test indicates that **B94** starts decomposing after exposing the films to 100 °C for 1 h, thus **B94** exhibits limited thermal stability. For RH%, **B94** shows higher stability when exposed to lower humidity conditions (see Figures S25 and S26 in the Supporting Information).

## 3. Conclusions

We have reported the photolithographic fabrication of oriented MOF micropatterns from oriented MOF films. The microfabrication process employs a resist-free lithography technique as the MOF acts as a positive tone resist. To impart X-ray sensitivity to the MOF film without altering the crystalline orientation, we combined the heteroepitaxial ceramic-to-MOF conversion approach with the mixed-linker strategy to afford the formation of a MOF film $Cu_2L_2DABCO$ (L = BDC/Br$_2$BDC). A sample prepared with 6% BDC and 94% Br$_2$BDC (here named **B94**) afforded the synthesis of continuous polycrystalline MOF films with 3D oriented crystals. This mixed ligand MOF system undergoes chemical and structural changes when exposed to X-ray radiation: when the irradiated regions are exposed to a developing solution, a spatially localized dissolution is triggered in tens of seconds. In the masked regions, the MOF film properties remain unchanged, and crystallinity, orientation, and pore access are retained for the MOF micropatterns. The immobilization of dye molecules within the oriented pore channels of the MOF pattern engenders a spatially controlled anisotropic fluorescent response. We envisage that the here proposed proximity lithography protocol, which combines precisely oriented MOF films with micropatterning, will progress the integration of MOF components with anisotropic functional properties into miniaturized devices.

## 4. Experimental Section

*Materials*: 1,4-Benzenedicarboxylic acid (BDC), DABCO, BODIPY, ethanol (99.7%), methanol, and acetic acid (99%), CHCl$_3$ were purchased from Sigma-Aldrich. 2,5-Dibromoterephtalic acid (Br$_2$BDC) was purchased from abcr. The Cu(OH)$_2$ nanobelts were prepared according to the literature.[15] All the reagents were used without further purification.

*Synthesis of $Cu_2[(Br_2BDC)_x(BDC)_{1-x}]_2DABCO$ (**B0, B94, B100**; where x = 0, 0.94, and 1, Respectively) Films from Cu(OH)$_2$ Nanobelts*: A film of aligned Cu(OH)$_2$ NBs was deposited onto a Si substrate (1.5 × 1.5 cm$^2$) following the automatic protocol previously reported by the research group (see the Supporting Information for details).[16]

*Synthesis of B0*: The ceramic-to-MOF converting solution was prepared by dissolving BDC (11.03 mg, 6.64 mм) and DABCO (30 mg, 26.74 mм) in 10 mL of methanol. The resultant mixture was sonicated for 10 min. Then, a film of aligned Cu(OH)$_2$ NBs was immersed into the converting solution. The closed vial was placed into an oven at 70 °C for 1 h. Afterward, the converted film was removed from the reaction medium, washed with ethanol, and dried under N$_2$ flow.

*Synthesis of B94*: The ceramic-to-MOF converting solution was prepared by mixing Br$_2$BDC (20.17 mg, 6.22 mм), DABCO (30 mg, 26.74 mм), and BDC (0.7 mg, 0.42 mм) in 10 mL of methanol. The resultant mixture was sonicated for 10 min. Then, a film of aligned Cu(OH)$_2$ NBs was immersed into the converting solution. The closed vial was placed into an oven at 70 °C for 1 h. Afterward, the converted film was removed from the reaction medium, washed with ethanol, and dried under N$_2$ flow.

*Synthesis of B100*: The ceramic-to-MOF converting solution was prepared by dissolving Br$_2$BDC (21.51 mg, 6.64 mм) and DABCO (30 mg, 26.74 mм) in 10 mL of methanol. The resultant mixture was sonicated for 10 min. Then, a film of aligned Cu(OH)$_2$ NBs was immersed into the converting solution. The closed vial was placed into an oven at 70 °C for 1 h. Afterward, the converted film was removed from the reaction media, washed with ethanol, and dried under N$_2$ flow.

*In Situ Encapsulation of BODIPY within B94 (**encBPY@B94**)*: First, a stock solution of BODIPY (0.81 mм) was prepared by adding 4 mg of BODIPY in 20 mL of MeOH, the resultant mixture was sonicated for 20 min to ensure the complete dissolution of BODIPY. Similarly, a stock solution of BDC (4.21 mм) was prepared by dissolving 14 mg of BDC in 20 mL of MeOH. The ceramic-to-MOF converting solution was prepared by dissolving the Br$_2$BDC (20.17 mg) and DABCO (30 mg) in a mixture of BODIPY (8 mL) and BDC (1 mL) stock solutions. The resultant mixture was sonicated for 5 min; then, a total volume of 10 mL was reached by adding 1 mL of MeOH. A film of aligned Cu(OH)$_2$ NBs was immersed into 10 mL of the converting solution. The closed vial was placed into an oven at 70 °C for 1 h. Then, the MOF film was removed from the reaction medium, washed with ethanol, and dried under N$_2$ flow.

*Activation of the MOF Film B94*: First, a solvent exchange procedure took place by immersing the MOF films in 5 mL of dry CHCl$_3$ for 5 min. Then, the sample was removed and dried under Ar flux to avoid water condensation. This procedure was repeated 3 times. Then, the film was placed under vacuum (7 mbar) and heated up at 120 °C, using a ramp of 5° min$^{-1}$. The sample was kept under these conditions for 3 h.

*Infiltration of BODIPY in B94 (**postBPY@B94**)*: An activated film of **B94** was immersed in 5 mL of a BODIPY solution (0.24 mм) prepared in dry CHCl$_3$. The vial was kept standing at room temperature for 12 h. Afterward, the film was removed from the solution, rinsed with CHCl$_3$, and dried under N$_2$ flow.

*DXRL Patterning Conditions*: The X-ray irradiation experiments were conducted at the DXRL beamline of Elettra-Sincrotrone Trieste (Italy), with synchrotron operating at 2.4 GeV.[38] To evaluate the sensitivity of the MOF films to X-ray radiation, each sample was exposed to incremental amounts of X-ray radiation: 291, 437, 874, 1748, 3497, and 6995 J cm$^{-2}$ through a mask that exposed only half of the sample (see the Supporting Information for details). The selected dose for patterning was then used with a lithography mask featuring exposed micrometric regions of different shapes and sizes (Figure S6, Supporting Information).

For the etching of the exposed samples, a developer solution composed of methanol (9 mL), water (1 mL), and acetic acid (0.02 mL, 35 mm) was used. The exposed samples were immersed in the developer for 40 s, then removed and immersed in ethanol for 10 s to rapidly quench the reaction, and finally dried under $N_2$ flow.

*Widefield Fluorescence Microscopy*: All experiments were performed in a widefield microscope built on an inverted Olympus IX83 body for epifluorescence configuration. For excitation, a 488 nm diode laser (iBeam Smart TOPTICA) was used. Spectral filtering of the laser line was performed using a cleanup filter (ZET488/10 Chroma). The orientation of the linearly polarized laser light (LPVISC100-MP2, Thorlabs) was controlled using rotating $\lambda/2$ waveplate (B-Halle, #RAC 3.2.10) mounted on a motorized positioner (OWISoft DMT65; PS10-32). The laser light was then focused by two lenses (AC508-100-A-ML and AC254-030-A-ML, Thorlabs) into the back focal plane of a 40× air objective (numerical aperture 0.95, working distance 0.18 mm, UPLSAPO40×2 Olympus). The waist of excitation beam was 69 µm on the sample plane. Excitation and detection paths were separated using a dichroic mirror (ZT488rdc-UF2, Chroma). Detection in the range $\lambda > 500$ nm was achieved using an emission filter (ET500lp Chroma). Videos were recorded with a complementary metal-oxide semiconductor camera (Orca Fusion Hamamatsu). Data acquisition was performed using the open-source software Micro-Manager.[39]

## Supporting Information

Supporting Information is available from the Wiley Online Library or from the author.

## Acknowledgements

## Conflict of Interest

The authors declare no conflict of interest.

## Data Availability Statement

The data that support the findings of this study are available from the corresponding author upon reasonable request.

## Keywords

anisotropic properties, metal–organic frameworks, micropatterning, MOF thin films, oriented MOFs, photonic devices

[1] W. Xu, B. Tu, Q. Liu, Y. Shu, C.-C. Liang, C. S. Diercks, O. M. Yaghi, Y.-B. Zhang, H. Deng, Q. Li, *Nat. Rev. Mater.* **2020**, *5*, 764.

[2] S. Kitagawa, R. Kitaura, S. Noro, *Angew. Chem., Int. Ed.* **2004**, *43*, 2334.

[3] W.-H. Deng, M.-S. Yao, M.-Y. Zhang, K. Otake, B. Wang, C.-S. Li, G. Xu, S. Kitagawa, *Natl. Sci. Rev.* **2022**, *9*, nwac143.

[4] W. Zhan, Q. Kuang, J. Zhou, X. Kong, Z. Xie, L. Zheng, *J. Am. Chem. Soc.* **2013**, *135*, 1926.

[5] I. Stassen, N. Burtch, A. Talin, P. Falcaro, M. Allendorf, R. Ameloot, *Chem. Soc. Rev.* **2017**, *46*, 3185.

[6] W. P. Lustig, S. Mukherjee, N. D. Rudd, A. V. Desai, J. Li, S. K. Ghosh, *Chem. Soc. Rev.* **2017**, *46*, 3242.

[7] M. Krishtab, I. Stassen, T. Stassin, A. J. Cruz, O. O. Okudur, S. Armini, C. Wilson, S. De Gendt, R. Ameloot, *Nat. Commun.* **2019**, *10*, 3729.

[8] M. Usman, S. Mendiratta, K.-L. Lu, *Adv. Mater.* **2017**, *29*, 1605071.

[9] O. Dalstein, D. R. Ceratti, C. Boissière, D. Grosso, A. Cattoni, M. Faustini, *Adv. Funct. Mater.* **2016**, *26*, 81.

[10] P. Falcaro, R. Ricco, C. M. Doherty, K. Liang, A. J. Hill, M. J. Styles, *Chem. Soc. Rev.* **2014**, *43*, 5513.

[11] J. Liu, C. Wöll, *Chem. Soc. Rev.* **2017**, *46*, 5730.

[12] G. Lu, O. K. Farha, W. Zhang, F. Huo, J. T. Hupp, *Adv. Mater.* **2012**, *24*, 3970.

[13] A. Bétard, R. A. Fischer, *Chem. Rev.* **2012**, *112*, 1055.

[14] Y. Lin, W. Li, Y. Wen, G. Wang, X. Ye, G. Xu, *Angew. Chem., Int. Ed.* **2021**, *60*, 25758.

[15] P. Falcaro, K. Okada, T. Hara, K. Ikigaki, Y. Tokudome, A. W. Thornton, A. J. Hill, T. Williams, C. Doonan, M. Takahashi, *Nat. Mater.* **2017**, *16*, 342.

[16] M. Linares-Moreau, L. A. Brandner, T. Kamencek, S. Klokic, F. Carraro, K. Okada, M. Takahashi, E. Zojer, C. J. Doonan, P. Falcaro, *Adv. Mater. Interfaces* **2021**, *8*, 2101039.

[17] P. Falcaro, D. Buso, A. J. Hill, C. M. Doherty, *Adv. Mater.* **2012**, *24*, 3153.

[18] Y. Miao, D. T. Lee, M. D. de Mello, M. Ahmad, M. K. Abdel-Rahman, P. M. Eckhert, J. A. Boscoboinik, D. H. Fairbrother, M. Tsapatsis, *Nat. Commun.* **2022**, *13*, 420.

[19] C. L. Ruiz-Zambrana, M. Malankowska, J. Coronas, *Dalton Trans.* **2020**, *49*, 15139.

[20] J. Reboul, S. Furukawa, N. Horike, M. Tsotsalas, K. Hirai, H. Uehara, M. Kondo, N. Louvain, O. Sakata, S. Kitagawa, *Nat. Mater.* **2012**, *11*, 717.

[21] A. Razmjou, M. Asadnia, O. Ghaebi, H.-C. Yang, M. E. Warkiani, J. Hou, V. Chen, *ACS Appl. Mater. Interfaces* **2017**, *9*, 38076.

[22] T. Ito, S. Okazaki, *Nature* **2000**, *406*, 1027.

[23] Y. Wang, I. Fedin, H. Zhang, D. V. Talapin, *Science* **2017**, *357*, 385.

[24] R. Kumar, N. Singh, C. K. Chang, L. Dong, T. K. S. Wong, *J. Vac. Sci. Technol., B: Microelectron. Nanometer Struct.–Process., Meas., Phenom.* **2004**, *22*, 1052.

[25] S. Takei, *Appl. Phys. Express* **2018**, *11*, 086501.

[26] S.-W. Lee, M. Muoth, T. Helbling, M. Mattmann, C. Hierold, *Carbon* **2014**, *66*, 295.

[27] M. Tu, B. Xia, D. E. Kravchenko, M. L. Tietze, A. J. Cruz, I. Stassen, T. Hauffman, J. Teyssandier, S. De Feyter, Z. Wang, R. A. Fischer, B. Marmiroli, H. Amenitsch, A. Torvisco, M. d. J. Velásquez-Hernández, P. Falcaro, R. Ameloot, *Nat. Mater.* **2021**, *20*, 93.

ADVANCED
SCIENCE NEWS

www.advancedsciencenews.com

ADVANCED
MATERIALS

www.advmat.de

[28] *CRC Handbook of Chemistry and Physics* (Ed: W. M. Haynes), CRC Press, Boca Raton, FL, USA **2014**.

[29] X.-J. Yu, Y.-M. Xian, C. Wang, H.-L. Mao, M. Kind, T. Abu-Husein, Z. Chen, S.-B. Zhu, B. Ren, A. Terfort, J.-L. Zhuang, *J. Am. Chem. Soc.* **2019**, *141*, 18984.

[30] T. Toyao, K. Liang, K. Okada, R. Ricco, M. J. Styles, Y. Tokudome, Y. Horiuchi, A. J. Hill, M. Takahashi, M. Matsuoka, P. Falcaro, *Inorg. Chem. Front.* **2015**, *2*, 434.

[31] K. I. Hadjiivanov, D. A. Panayotov, M. Y. Mihaylov, E. Z. Ivanova, K. K. Chakarova, S. M. Andonova, N. L. Drenchev, *Chem. Rev.* **2021**, *121*, 1286.

[32] H. T. Varghese, C. Y. Panicker, D. Philip, K. Sreevalsan, V. Anithakumary, *Spectrochim. Acta, Part A* **2007**, *68*, 817.

[33] K. Tan, N. Nijem, P. Canepa, Q. Gong, J. Li, T. Thonhauser, Y. J. Chabal, *Chem. Mater.* **2012**, *24*, 3153.

[34] K. Okada, M. Nakanishi, K. Ikigaki, Y. Tokudome, P. Falcaro, C. J. Doonan, M. Takahashi, *Chem. Sci.* **2020**, *11*, 8005.

[35] O. Dalstein, E. Gkaniatsou, C. Sicard, O. Sel, H. Perrot, C. Serre, C. Boissière, M. Faustini, *Angew. Chem., Int. Ed.* **2017**, *56*, 14011.

[36] S. Klokic, D. Naumenko, B. Marmiroli, F. Carraro, M. Linares-Moreau, S. D. Zilio, G. Birarda, R. Kargl, P. Falcaro, H. Amenitsch, *Chem. Sci.* **2022**, *13*, 11869.

[37] A. K. Adamczyk, T. A. P. M. Huijben, M. Sison, A. Di Luca, G. Chiarelli, S. Vanni, S. Brasselet, K. I. Mortensen, F. D. Stefani, M. Pilo-Pais, G. P. Acuna, *ACS Nano* **2022**, *16*, 16924.

[38] F. Pérennès, F. De Bona, F. J. Pantenburg, *Nucl. Instrum. Methods Phys. Res., Sect. A* **2001**, *467–468*, 1274.

[39] A. Edelstein, N. Amodaj, K. Hoover, R. Vale, N. Stuurman, *Curr. Protoc. Mol. Biol.* **2010**, *92*, 14.20.1.

**2211478 (10 of 10)**